NDT&E International 67 (2014) 24–30

Contents lists available at ScienceDirect

NDT&E International

journal homepage: www.elsevier.com/locate/ndteint

Localisation of defects with time and frequency measurements using pulsed arrays

Samuel Hill [a,*], Steve Dixon [a,b]

[a] Department of Physics, University of Warwick, Gibbet Hill Road, Coventry CV4 7AL, United Kingdom
[b] School of Engineering, University of Warwick, Gibbet Hill Road, Coventry CV4 7AL, United Kingdom

ARTICLE INFO

Article history:
Received 28 December 2013
Received in revised form
19 June 2014
Accepted 28 June 2014
Available online 5 July 2014

Keywords:
EMAT
Array
Diffraction
Ultrasonic scattering

ABSTRACT

The frequency dependent directivity of the periodic permanent magnet transducer is used to extract information about the position of any discontinuities present in a sample. Two approaches are used: narrowband excitation and broadband pulsed generation. Simultaneous narrowband excitation, with the appropriate frequency, can be used to steer the ultrasound to a particular angle. Broadband excitation emits a wavefront that extends over a large range of angles, with the frequency of the wavefront varying smoothly as a function of angle. Using these two approaches, two-dimensional maps of any defects present in the sample can be obtained.

1. Introduction

Recently published work has demonstrated how a wavefront with a frequency dependent angle of propagation can be generated by simultaneously activating a periodic array of ultrasonic emitters [1]. By utilising this physical phenomenon, the location of a discontinuity can be ascertained by measuring the frequency of the scattered signal, as well as the time-of-flight. A new send–receive configuration is presented here, whereby the data obtained from such a broadband pulsed array can be processed to form a two-dimensional map of the location of defects that may be present in a sample. This broadband approach is compared to the established narrowband excitation technique. This narrowband approach can steer an ultrasonic beam to a particular angle by exciting the array with a low bandwidth signal of a particular frequency [2–4]. The ultrasonic beam can be swept over a range of angles by simply varying the excitation frequency. The accuracy and the precision of the localisation of defects obtained from these approaches are compared using calibration and realistic samples by interrogating them with Shear Horizontal (SH) waves.

SH waves are becoming a useful tool for ultrasonic inspection applications as they have a number of advantageous qualities. For instance, if a SH wave is obliquely incident on a free surface, it will not mode convert to either longitudinal or shear vertical (SV) waves [5]. This means that the received signals are easier to analyse, as there is only one type of wave present, as well as minimising energy loss at the boundary of the sample. It has also been shown that SH waves can pass through austentic welds with limited distortion when compared to longitudinal and shear vertical (SV) waves [6], as a consequence of the typical microstructure [7]. However, the widespread utilisation of SH waves in non-destructive testing has been limited by the inability to efficiently generate SH waves using piezoelectric transducers [5]. Shear energy cannot easily propagate through a low viscosity fluid, such as those used for ultrasonic couplant between a piezoelectric transducer and the sample. Horizontal polarisation shear waves are also difficult to excite via mode conversion from a wedge.

However, SH waves can be easily excited using electromagnetic acoustic transducers (EMAT), specifically using a periodic permanent magnet (PPM) EMAT [8,5]. A PPM EMAT consists of an array of magnets, which alternate polarity with their nearest neighbours, and a racetrack coil that is excited with an alternating current. The exact configuration can be seen in Fig. 1. For a non-ferromagnetic sample, the Lorentz force dominates [9]: setting up alternating forces, arising as a result of the interaction between the induced eddy currents and the static magnetic field, within the skin depth of the sample [10]. It is these alternating Lorentz forces that generate the SH wave, which will have a wavelength on the surface equal to the periodic distance of the array, d, which is twice the pitch of the PPM array. The PPM transducer also benefits from the usual advantages of EMATs, such as not requiring any direct contact with the sample, and the ability to generate ultrasound of a single polarisation [11].

It is possible to use the periodic structure of the magnet array in a PPM EMAT to control the angle at which the SH waves propagate [2,3,12]. Phased array methods [13,14] rely on precisely activating the individual array elements with a time delay in order

* Corresponding author: Tel.: +44 2476522248.
E-mail address: Samuel.Hill@warwick.ac.uk (S. Hill).

http://dx.doi.org/10.1016/j.ndteint.2014.06.008

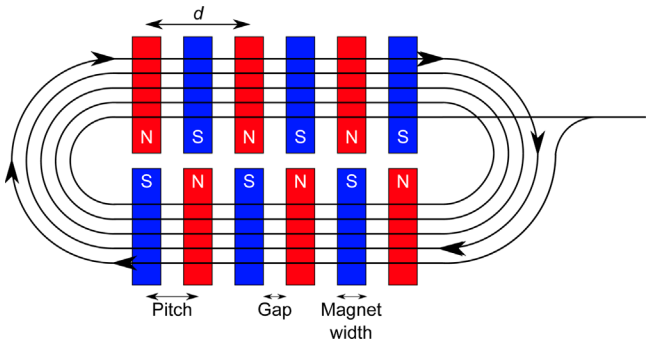

Fig. 1. PPM EMAT configuration, showing the magnet array and racetrack coil.

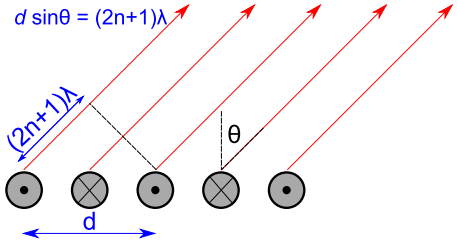

Fig. 2. Array configuration showing the condition for constructive interference.

to manipulate the ultrasonic beam. However, with a PPM EMAT, beam steering can be achieved by exciting all of elements simultaneously, with a narrow-band signal [15]. Consequently, it is possible to steer the ultrasonic beam without having the complication of requiring the individual control of each element in the array. This is described in more detail in Section 2.1. Section 2.2 explains how an array can be pulsed with a broadband signal to create a wavefront that covers a large angular region, with a frequency dependent on the angle of propagation. Experimental data is presented in Section 3 to demonstrate how PPM EMATs and SH waves can be used to detect and locate defects. For the frequency steered array, the beam can be used to sweep through a range of angles, by changing the driving frequency, in order to create a 'sector scan' image, whilst time–frequency analysis can be used to interpret data obtained from the pulsed array. Due to the frequency variation as a function of angle, any wave that has been scattered from the original pulsed array wavefront will have a unique arrival time and frequency. This can be used to locate the defect by converting the time of flight to a radial distance, with the frequency of the scattered wave being related to the angle of the defect [1].

2. Theory

2.1. Frequency steered arrays

The alternating Lorentz forces generated by the PPM EMAT act to generate SH waves on the sample surface, with the periodicity of the EMAT array defining the wavelength of the generated waves. The spatial periodicity of the PPM EMAT can also be used to generate SH waves that are steered so that they propagate at an angle to the sample surface. Ultrasonic steering using simultaneous excitation is achieved due to interference effects [15]. This constructive interference occurs when the path length difference between waves from two neighbouring elements of the same polarity is equal to an odd-integer number of wavelengths. This is a condition that changes with frequency, and hence the SH beam can be steered by simply varying the input signal frequency. The condition for constructive interference can be calculated as

$$d \sin \theta = (2n+1)\lambda \quad (1)$$

Here, d is the periodic distance of the array, λ is the ultrasonic wavelength, n is the order of interference and θ represents the angle at which the ultrasonic beam is steered. Therefore it is possible to direct the ultrasonic beam to an angle θ by driving the PPM EMAT with a tone-burst signal of a particular frequency, ν (associated with a wavelength: $\nu = c/\lambda$). The ultrasonic beam can be swept over a large range of angles, simply by varying the input frequency. The beam can be steered from the surface, at $\theta = \pi/2$, up to an angle at which the first grating lobe appears. For the array shown in Fig. 2, the next order of interference occurs when $\lambda = d/3$ [1]. So, in the angular range $20^\circ \leq \theta \leq 90^\circ$, only the lowest order diffraction term is satisfied, meaning that there is only one main beam. Frequency domain models can be constructed to calculate not only the steering angle, but also the other important parameters such as the beam shape and width, as well as other characteristics such as side lobes [15]. Knowing the total frequency dependent directivity of the array means that any received signal can be correctly interpreted.

The ability to steer the ultrasonic beam provides the opportunity to create ultrasonic images. For example, it is possible to perform a sector scan by simply repeating the measurements at different frequencies. By varying the frequency between c/d and $3c/d$, the main beam will be steered from 90° to 20°. The resultant A-scans obtained from the frequency sweep can be combined into a single 'image', showing two dimensional information (time–frequency, or radial–angular position) about any defect that may be present.

2.2. Pulsed arrays

When simultaneously exciting all the elements of the array with a pulse of the correct frequency bandwidth, a wavefront is generated over a large solid angle. The frequency of the wavefront varies with the angle of propagation, with the same dependence between frequency and angle as was seen for the frequency steering. As with the frequency steered arrays, constructive interference occurs at an angle for which the diffraction grating equation (Eq. (1)) is satisfied. However, as the input signal contains a range of frequencies, this condition is satisfied continuously over a wide range of angles. As this change in frequency is continuous and monotonic, it can be used to locate the position of a scatterer. This is because the frequency encapsulates the angular position of the scatterer, whilst the time of flight can be used to determine the radial distance of the scattering body. The wavefield can also be used to interrogate a large section of the sample in a single pulse, due to the large angular area that it covers.

Analytic and finite element (FE) modelling techniques can be used to gain more information about the wavefront, such as how it evolves in time, as well as confirming the angular dependence of the frequency [1]. The analytic model, using a simplified Huygens approach, has the advantage of being able to extract the key physical characteristics of the wave. The simulated wave displacement is shown in Fig. 3 as an SH wave generated by an array with $d = 10$ mm operating on aluminium ($c_s = 3111$ ms^{-1}). It demonstrates that the wavefront extends over a large angular region, from the surface, at $\theta = 90^\circ$, up to around $\theta = 20^\circ$. In this angular range, the frequency of the wave is changing: from low frequency ν_0 on the surface, up to $3\nu_0$ at $\theta = 20^\circ$. This means that an angular region of around 70° can be covered with a single pulse. The exact frequency variation can be seen in Fig. 4, which is in accordance with the expected diffraction grating behaviour. This allows us for easy conversion between the measured peak frequency of any scattered signals and the angle from which they originated.

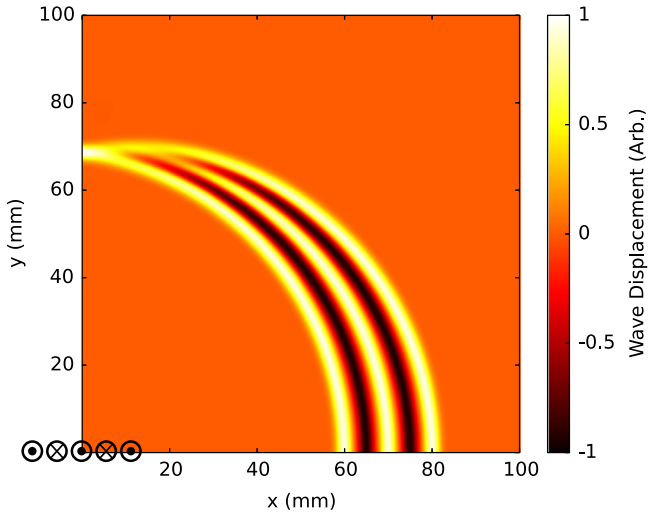

Fig. 3. Analytic model of the out of plane displacement in an aluminium sample from an array with $d = 10$ mm, 22.5 μs after the array was pulsed. The array is shown in the bottom left corner, and indicates the polarity of the array elements.

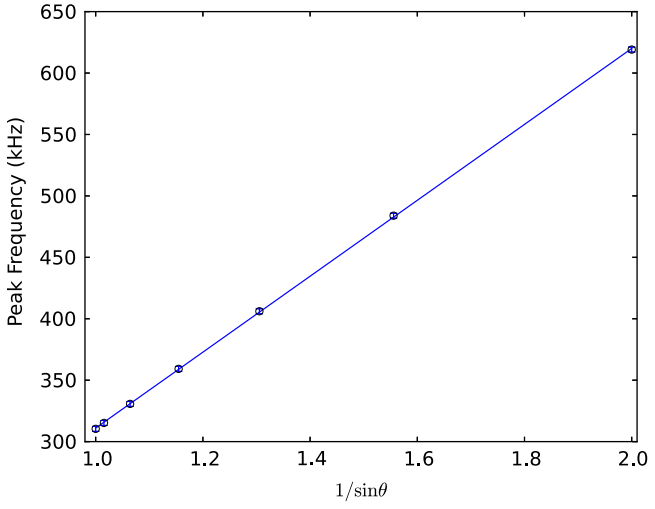

Fig. 4. Angular dependence of the centre frequency of the wave shown in Fig. 3. Error bars are plotted, and are associated with determining the peak of the frequency spectra at each angle. These uncertainties are around the size of the markers used on the graph.

3. Experiment

3.1. Frequency steered results

As discussed in Section 2.1, it is possible to steer the ultrasonic beam to a particular angle simply by driving the array with a narrow-band frequency signal. As one can steer the ultrasound to a desired angle, it is possible to utilise sector scan imaging, as has been implemented with phased arrays [16,17]. By varying the input frequency during a measurement, it is possible to sweep the ultrasonic beam over a range of angles. Due to the presence of higher order diffraction terms, there is a single main beam in the angular region $20^\circ \leq \theta \leq 90^\circ$; outside of this angular region there will be third order (or higher) diffraction terms adding other grating lobes. By varying the frequency between the 'fundamental' frequency, $\nu_0 = c_S/d$, and three times this 'fundamental' frequency, a large angular region can be inspected [1,15].

By using the EMAT in a pulse-echo configuration, any ultrasound scattered from any discontinuities present will be received as an echo by the same PPM EMAT used for generation. Whilst using the EMAT in a pulse-echo configuration resulted in a reduction of signal amplitude, mainly due to the electrical ringing of the amplifier connected to the transducer [12], there are a number of benefits. For instance, it simplifies the geometry of the situation, in terms of locating the defect, when compared to using a separate transducer. Any scattered wave will come back to the transducer as a backscattered wave – meaning that the time of flight of the wave can be simply related to the radial distance of the discontinuity, and the angle of peak echo amplitude corresponds to the angle of the defect. Due to reciprocity, the frequency dependence of the directivity also applies in reception, meaning that any non-backscattered signals are partially filtered. This has the effect of enhancing the relationship between the frequency of the scattered wave and the angle of propagation of the wave, thereby reducing the complexity in analysing the signals. It was found that the pulse-echo signal could be recovered by using a simple background subtraction to remove the coherent ringing signal of the EMAT. The background signals were obtained by rotating the EMAT by 45°, which ensured that there were no reflected signals in the time window of interest, and therefore only contained the ringing of the transducer. A frequency domain band-pass filter was applied to the signals, so that only frequencies in the range of interest (passband: 400 kHz–1.5 MHz) remained, which clearly reveals the echoes. The amplitude of these echoes should reach a maximum when the array is driven at a frequency that corresponds to the angular position of the defect. The peak in the two dimensional 'image', constructed by combining the individual A-scans from the frequency sweep, can be used to localise the defect in space; the time of flight value can be converted into a radial distance, whilst the angular position can be determined by the excitation frequency at which the peak occurs.

The test specimen used was a rectangular aluminium bar, with a cross-sectional area of 59×59 mm^2, as shown in Fig. 5. The bar had several notches cut out of it, which act as discontinuities to scatter the ultrasound. The largest was the 10 mm deep slot, and this was the source of the primary reflections seen in the experimental data. A six element PPM EMAT, with an element size of 2.5 mm and a pitch of 3 mm, was used in a pulse-echo configuration and placed at the end of the bar. Such a 3 mm pitch PPM EMAT, operating on aluminium ($c_s = 3111$ ms^{-1}), generates a surface shear wave with a frequency of 518 kHz. Hence, the array was excited with a narrow-band five cycle sine wave, with the frequency of the excitation signal varying from 520 kHz to 1.07 MHz in increments of 10 kHz; this ensured that the inspection had good angular coverage, with good angular resolution. As described, the ringing of the transducer obscured some of the backscattered signals. However, as the ringing was clearly coherent, it could easily be removed by a simple background subtraction – with a background signal needed for each drive frequency. The data, after being baseline subtracted and band-pass filtered, can be seen in Fig. 6. A number of reflections of various amplitudes can be seen in the data, with the amplitudes of the backscattered signals changing with frequency. Most of the large amplitude signals are from the 10 mm notch; with the first signal to arrive due to the wave travelling along the surface and being reflected back. The signals that arrive later are also signals scattered by the 10 mm

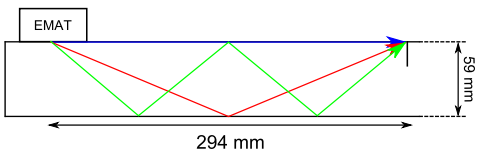

Fig. 5. Schematic experimental diagram, illustrating a number of possible ultrasonic paths to the 10 mm deep notch.

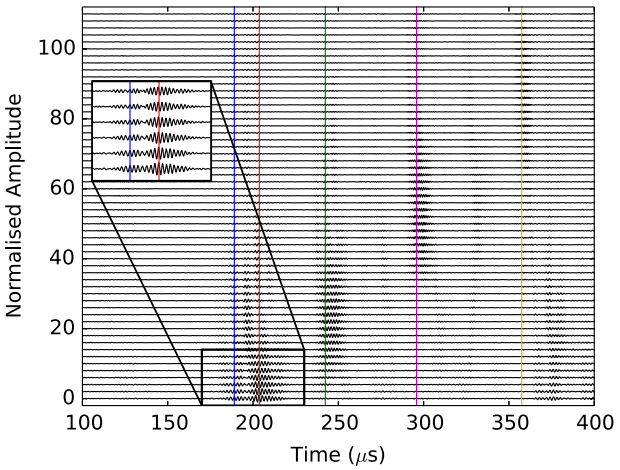

Fig. 6. Experimental backscatter signals with the expected time of flights, calculated from geometry, overplotted on the data as vertical lines. The inset shows a zoomed version of the six lowest frequencies (520–570 kHz excitation frequencies), which highlights the first two reflected signals.

notch, but have taken a multi-skip path. This is due to the steering of the ultrasonic beam: with the higher frequency signals being steered to a multi-skip path to the notch. Importantly, each reflection has a unique path length and angle of propagation, meaning that each signal should also have a unique time of flight and frequency.

The length and the angle of propagation of the expected paths taken by the ultrasound can be calculated from Fig. 5, using simple geometry. The expected path lengths are converted to times of arrival values, and are overplotted in Fig. 6 as vertical lines. This shows good alignment between the observed echoes and their expected time of flight, demonstrating that the radial position can be ascertained with a good degree of accuracy. The smaller amplitude signals that can be seen between the marked, higher amplitude signals simply come from other notches on the bar, whilst the signal at 375 μs in the lower frequency scans is a multiple reflection of the surface echo originally seen at 189 μs. In addition to determining the radial positions of the defects, it is also possible to try and infer their angular positions. By time windowing the data in order to isolate each individual echo, it is possible to see how the amplitude of these echoes changes with frequency. It would be expected that the amplitude of the echo will be at a maximum for a frequency that corresponds to a steering angle that matches the angular position of the defect. As the first two signals could not be clearly separated in time, only the last three marked echoes in Fig. 6 were time windowed. The root mean square (RMS) amplitude of each of the echoes is plotted as a function of frequency, which can be related to the steering angle using Eq. (1). These results are shown in Fig. 7, which exhibits a clear variation in amplitude as a function of frequency for all of the scattered signals. The measured radial and angular co-ordinates, obtained from the time of flight and frequency measurements, are given in Table 1. It can be seen that there is generally good agreement between the measured path length and angle and the geometrically calculated values. Some of the small discrepancies may arise because the notch has a relatively large length, whereas the geometric calculations assume a point reflection on the surface. The finite length of the notch means that, in fact, a range of paths is valid as reflections from the face of the notch, rather than just the intersection of the notch with the surface of the sample.

From Fig. 7, it is also apparent that the ultrasonic beam width changes as a function of angle, with the beam being narrow at the lower angles, whilst spreading the beam out over a large range for the larger angles towards the surface. This is a consequence of the inverse proportionality between frequency and angle that can be seen from Eq. (1), and can also be seen in the directivity modelling [15]. This has the effect of creating an angularly dependent resolution; a smaller beam width at the lower angles (higher frequencies) leads to a better resolution than at higher angles (lower frequencies), where the ultrasound is 'steered' over a much larger range of angles.

The driving signal obviously also has an effect on the beam width that is achieved by frequency steering. By driving the array with a narrow bandwidth signal, the ultrasonic beam will be steered over a very narrow range of angles as there are only few frequencies present, and so there is only a limited range of angles for the signal to constructively interfere. However, a narrow bandwidth signal necessarily implies that it will have a large temporal range, hence leading to poor axial resolution. Therefore, there is an explicit compromise between angular and axial resolutions caused by time–frequency duality; increased angular resolution directly causes a reduction in the axial resolution that could be achieved and vice versa [18]. Nevertheless, a 5 cycle toneburst appears to be a good compromise, with reasonable axial and angular resolutions being achieved in this case.

3.2. Pulsed results

As well as using the frequency steering properties of the PPM array to create a frequency-based sector scan, it is also possible to use the pulsed properties of the array to inspect a component. Pulsing the array has the benefit of generating a wave that covers a large angular range, meaning that a greater region is simultaneously inspected. With the frequency steering method, 56 measurements were required, but the pulsed array can cover the same angular region with just a single measurement (although the number of measurements needed for each method is doubled by the necessity for background data for the baseline subtraction). For the pulsed experiment, the setup is the same as in Section 3.1, with the array used in pulse-echo to inspect the same sample as shown in Fig. 5. However, this time, after being pulsed with a 800 kHz single cycle sine signal, the wavefront covers all of the paths simultaneously, meaning that all of the echoes are present in a single time-domain signal, or A-scan. Therefore, a form of time–frequency analysis is required in order to localise the individual reflections in both time and frequency, which will, in turn, lead to the localisation of the defect paths in both radial distance and angular position. A spectrogram, calculated as the squared magnitude of a short-time Fourier Transform (STFT) [19,20], with a Hann function as the windowing function, is used to analyse the obtained time domain signal. Both the time domain A-scan and the spectrogram are shown in Fig. 8. The spectrogram expands the A-scan to show the time-localised frequency, allowing the signals to be clearly resolved in both time and frequency. The location of the peaks in the spectrogram is related to the length and angle of the ultrasonic path to the defect, with the overlaid circles on the figure indicating the calculated time of flight and frequency from the expected path length and angle of propagation. Again, it can be seen that there is very good agreement, and that the pulsed method can localise defects very well, with the results shown in Table 2.

From comparing Tables 1 and 2, it can be seen that, whilst both methods appear to be accurate, the pulsed array results offer improved accuracy and precision. This can be explained by the fact that the pulsed wavefront is continuous over the entire angular range of interest, whereas the frequency steering method is effectively sampling the structure at discrete angles. This increased amount of information is reflected in improved resolution of the results obtained using the pulsed method. However, as observed

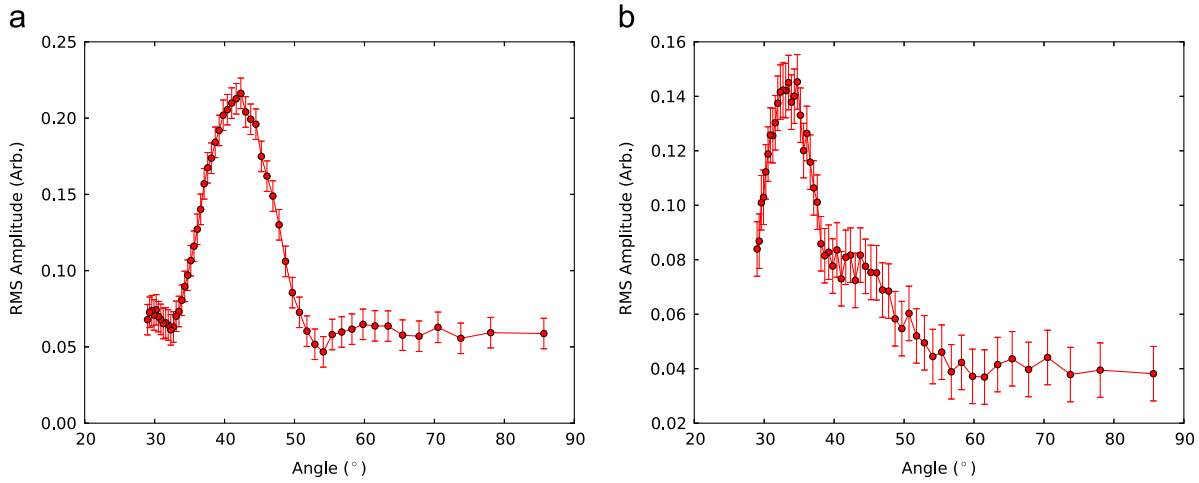

Fig. 7. Angular dependence of the amplitude of the scattered waves caused by the defects at (a) 40° and (b) 32°.

Table 1
Comparison between frequency sweep and calculated co-ordinates of five observed echoes.

Number of skips	Measured co-ordinates (r,θ)	Calculated co-ordinates (r,θ)
0	$(295.8 \pm 0.5\ \text{mm}, \text{n/a})$	$(294.0\ \text{mm}, 90.0°)$
1	$(316.5 \pm 0.5\ \text{mm}, \text{n/a})$	$(316.8\ \text{mm}, 68.1°)$
2	$(383.3 \pm 0.5\ \text{mm}, 54.3 \pm 3.0°)$	$(377.0\ \text{mm}, 51.2°)$
3	$(462.5 \pm 0.5\ \text{mm}, 41.1 \pm 1.6°)$	$(460.2\ \text{mm}, 39.7°)$
4	$(557.1 \pm 0.5\ \text{mm}, 32.8 \pm 1.0°)$	$(556.1\ \text{mm}, 31.9°)$

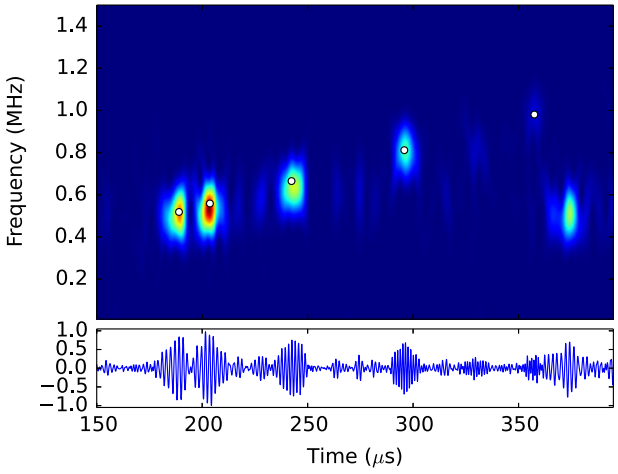

Fig. 8. Spectrogram (upper plot) and time domain signal (lower plot) showing the time localised frequency of the scattered signals. The circles that are plotted on the figure indicate the calculated time of flight and peak frequency of the waves taking the expected geometric paths shown in Table 2. The low frequency signal seen at 375 μs corresponds to a reflection of the surface wave from the end of the bar.

Table 2
Comparison between pulsed and calculated co-ordinates of five observed echoes.

Number of skips	Measured co-ordinates (r,θ)	Calculated co-ordinates (r,θ)
0	$(294.3 \pm 0.5\ \text{mm}, 87.8 \pm 7.2°)$	$(294.0\ \text{mm}, 90.0°)$
1	$(316.2 \pm 0.5\ \text{mm}, 72.5 \pm 0.9°)$	$(316.8\ \text{mm}, 68.1°)$
2	$(378.3 \pm 0.5\ \text{mm}, 52.6 \pm 0.5°)$	$(377.0\ \text{mm}, 51.2°)$
3	$(459.9 \pm 0.5\ \text{mm}, 39.7 \pm 0.2°)$	$(460.2\ \text{mm}, 39.7°)$
4	$(555.8 \pm 0.5\ \text{mm}, 31.8 \pm 0.5°)$	$(556.1\ \text{mm}, 31.9°)$

with the frequency sweep approach, the resolution of the pulsed approach also varies with angle. As explained previously, this is due to the relationship between angle and frequency; for a given

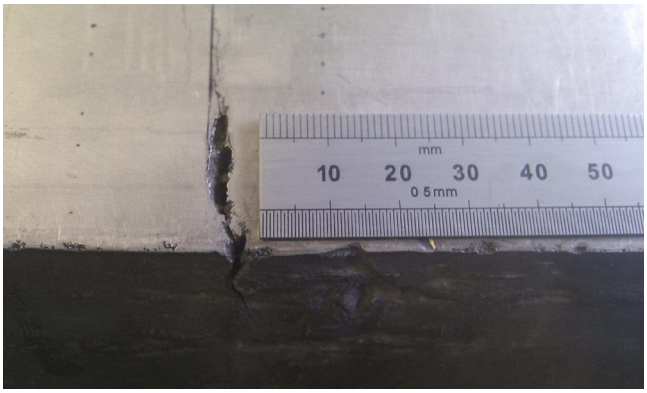

Fig. 9. Image of rough crack that is to be inspected.

change in frequency, the angle changes a lot more for the higher angles than it does for the lower ones. Therefore, the same uncertainty in frequency leads to a much greater angular uncertainty at higher angles than it does for the lower angles. The pulsed method is also able to achieve a good signal-to-noise ratio, with most of the echoes being clearly identifiable. Whilst the notch is large (10 mm), and therefore allows for a range of ultrasonic paths to be detected, it should also be noted that some of the echoes are travelling a round trip of over 1 m. This shows that the transducer is sufficiently efficient to generate a useful wave front over a large range of angles, despite having to spread the energy over such a large angular range.

3.2.1. *Pulsed results from rough defect*

For this pulsed array system to be a useful inspection technique, it has to be applicable not only to artificially cut notches, as seen in the previous section, but also to representative defects. As the pulsed method proved to be superior, in terms of both scan speed and result accuracy, only the pulsed approach was utilised here. The sample used was an aluminium billet with a rough crack, with depths varying between 2 mm and 20 mm [21], upon the surface of the sample, which can be seen in Fig. 9. Rough defects have a number of issues that could mean that the pulsed approach may no longer be applicable. Firstly, whereas the notches lead to high amplitude specular reflections, rough defects will diffusely scatter any incident ultrasound [22–24]. This diffuse scattering will lead to lower amplitude reflections, and hence indications from defects will be more difficult to detect. Secondly, the roughness of the defect may introduce frequency dependent scattering events,

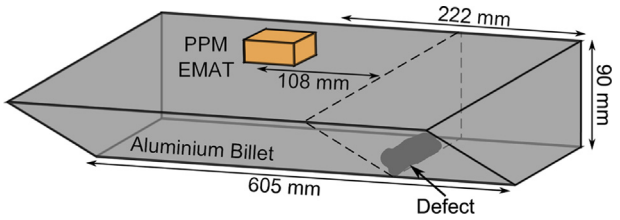

Fig. 10. Schematic diagram of the sample. The defect is located on the underside of the sample, and its position is indicated by the dashed line. The PPM EMAT is also indicated on the diagram, with the centre of the array 108 mm from the position of the defect.

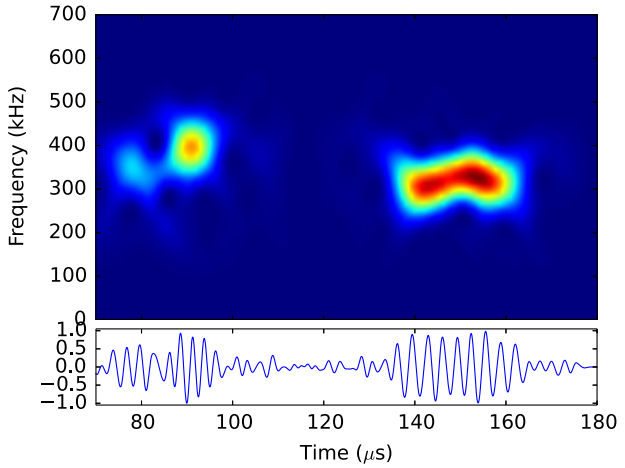

Fig. 11. Time domain signal (lower plot) and spectrogram (upper plot) showing the time localised frequency of reflections from the sample containing a rough crack. The reflections from the end of the sample, at times of approximately 140 μs and 155 μs, are not scattered signals from defects. The indication at 90 μs corresponds to the expected position of the defect.

which could cause an angular mis-location of a defect. Whilst most of the roughness associated with the defect shown in Fig. 9 will be on a scale much smaller than the wavelength of the ultrasound, it will still not act as a planar scatterer as was the case in Sections 3.1 and 3.2. Other studies [1], as well as the experimental results in Section 3.2, show no sign of scattering events significantly altering the frequency content of the pulse. However, there is no guarantee that a rough defect will not have any frequency dependent scattering interactions, and so this must be investigated.

The experimental geometry is shown in Fig. 10, with the defect location indicated on the top surface. This time a larger EMAT, with a pitch of 5 mm and element size of 4 mm, was used. The larger element size increases the generation area, which, in turn, increases the amplitude of the ultrasonic wavefront. In order to avoid any surface waves obscuring the reflected signal from the defect, the EMAT was placed on the bottom surface. By placing the EMAT on the bottom surface of the billet, any reflections from the defect will be separated in time from any much larger reflections from the end of the sample. It also ensures that these reflections will have distinct frequencies as well, as any wave restricted to the surface will have a frequency of 311 kHz, with any reflections from the bottom surface having a higher frequency than this. As before, the data was obtained from the PPM EMAT in pulse-echo mode. Background subtraction was again required, and the resultant data was band-pass filtered as in the previous sections. Again, the obtained time domain signal was analysed using a spectrogram to obtain a time–frequency map of the sample, with the same parameters used as in Section 3.2.

The resultant A-scan and the spectrogram can be seen in Fig. 11, with a number of indications visible from the scan. The indications between 140 μs and 160 μs are consistent, in both arrival time and frequency, with reflections from the end of the sample. However, there is one indication that cannot be explained by the geometry of the sample. This is the indication that peaks at 91.1 ± 0.3 μs in the time domain, with a frequency of 400 ± 5 kHz. Once these are transformed into spatial co-ordinates using the known wave speed, for the radial position, and the diffraction grating equation, for the angular position, it is found that the position of the defect was $(r, \theta) = (141.7 \pm 0.5\ \text{mm}, 51.0 \pm 1.0^\circ)$. As the defect was surface breaking, the distance from the EMAT to the defect could easily be measured, and was found to be $(r, \theta) = (140.9 \pm 1.0\ \text{mm}, 50.2 \pm 0.2^\circ)$. The pulsed array method agrees well with the known position of the defect, with both the radial and angular positions being within experimental error. From the accuracy of angular measurement, it is apparent that there is no strong frequency dependence in the scattering processes in the bandwidth. This does not mean that the scattering does not have any frequency dependence; it means that the variation in scattering is small enough over the bandwidth of the signal that the peak frequency of the signal has not been significantly altered by the scattering event. This adds confidence that the pulsed array system can be utilised in a wide range of non-destructive testing scenarios.

4. Conclusion

We have successfully demonstrated a new configuration for ultrasonic send–receive testing. By simultaneously exciting a periodic array of ultrasonic sources, it is possible to manipulate and alter the directivity of the array by carefully controlling the frequency content of the generation signal. The interference between the waves produced by each individual elements causes preferential propagation of ultrasound with a certain frequency along a particular angular path. The frequency–angle pair is given by the diffraction grating equation, and occurs when the spatial periodicity of the array and the wavenumber of the excitation signal overlap in the spatial frequency domain, meaning that there is a constructive interference of that signal at that particular angle. As this condition of constructive interference changes with frequency, ultrasonic beam steering and sector scans can be achieved by simply varying the frequency of the excitation signal. This removes the requirement to be able to individually control and phase each array element, thereby avoiding the need for expensive hardware. Another interesting phenomenon can be generated with the same array: a pulsed array wavefront, where the generated wavefront covers a large angular range, and has a smooth variation of frequency as a function of angle. This new effect, which can be generated by pulsing the array with a specific broadband signal, can be utilised to determine the location of a scatterer. As the frequency of the wavefront changes smoothly and continuously as a function of angle, the frequency of any scattered wave can be associated with the angular position of the discontinuity, whilst the radial position is simply related to the time of flight of the reflection.

Both the frequency sweep sector scan and the broadband pulsed method were used to inspect a machined aluminium sample, with a 10 mm notch acting as a defect. Whilst only one defect was present, there were are a number of multiple skip paths the ultrasound could take to the notch, due to the limited depth of the sample. This means the ability to detect and locate defects over a range of angles could be tested. The pulsed method has various advantages over the frequency sweep approach, namely that it can cover the same angular region with a single scan, whereas the frequency sweep approach requires multiple measurements over a range of different frequencies. The pulsed measurements also appear to have superior accuracy and resolution, with the resolution of the pulsed approach limited by frequency resolution of the

spectrogram, rather than the beam width, as is the case for the frequency steering. The pulsed wavefront is also continuous over the entire angular range of interest, meaning that more information is available than the frequency steering case, which effectively samples at discrete angles. Perhaps surprisingly, the drop in peak wave amplitude, associated with spreading the ultrasonic energy over a large range of angles, does not result in a dramatic reduction of the signal to noise ratio. This is mainly because the noise is distributed over a large range of frequencies, whereas the signal is obviously fairly narrowband in comparison.

As the pulsed array was shown to be superior to the frequency steering approach, it was used to inspect another sample with a real defect. It was shown that the combination of time of flight and frequency could still be used to locate this rough defect, despite the reduction the amplitude of any reflections. The rough defect also appeared to have no strong frequency dependence in its scattering processes, meaning that the frequency of the scattered wave can still be used to infer the angular position of a defect, even if it is not smooth. This demonstrates that the pulsed array method has the potential for the use on industrial samples.

Whilst simultaneously activated arrays can replicate some phased array modalities, it should be noted that the techniques can be complementary, and would be employed in differing scenarios. For example, phased arrays, and the Total Focusing Method (TFM) in particular, can create high resolution images with an excellent signal-to-noise ratio of around 40 dB [17]. However, this improved inspection accuracy comes at the expense of additional hardware and software complexity. While not being able to replicate the precision of TFM measurements, the broadband pulsed array has the benefit of being able to locate defects with a single measurement. In addition, as the wavefront is generated over a 70° angular range, a large volume can be inspected with a single measurement. It should also be noted that these benefits are obtained with a vast reduction in the system complexity; the array used in this work contained only six elements, which were pulsed simultaneously, which precludes the requirement for phased array hardware. In addition, the analysis of the pulsed array data is less computationally intensive than when compared to TFM; only a single time domain signal is required to locate a defect with a pulsed array, whereas N^2 measurements are recorded in a full matrix capture using an N element array. So, whilst the pulsed array system could be used to inspect a large volume for defects, if higher resolution measurements are needed then more complex array procedures are required.

There are a number of avenues to explore for future work, in particular the use of other time–frequency analysis methods. The STFT spectrogram was utilised here, as it is the simplest to implement. Whilst all of the echoes could be clearly resolved in both time and frequency, the spectrogram suffers from a fixed resolution, i.e. an increase of time resolution necessarily leads to a decrease in frequency resolution. Other methods of time–frequency analysis, such as discrete wavelet analysis, benefit from advantage of multi-resolution analysis, which offers improved temporal resolution of the high frequency components, and frequency resolution of the low frequency components [25,18,19]. Also, whilst the current work has utilised SH waves that are generated by EMATs, the physics that describes the pulsed array system is universal to other types of waves. Future work will include demonstrating this phenomenon with a number of other systems, for example using longitudinal ultrasonic waves or electromagnetic waves.

Acknowledgements

This work was financially supported by the UK Engineering and Physical Sciences Research Council (EPSRC) through the UK Research Centre in NDE (RCNDE). We would also like to thank Professor George Rowlands for many useful discussions and his valuable contributions to the project.

References

[1] Dixon S, Hill S, Fan Y, Rowlands G. The wave-field from an array of periodic emitters driven simultaneously by a broadband pulse. J Acoust Soc Am 2013;133(6):3692–9.
[2] Moran TJ, Panos RM. Electromagnetic generation of electronically steered ultrasonic bulk waves. J Appl Phys 1976;47(5):2225–7.
[3] Ohtsuka Y, Higashi M, Nishikawa M. Fundamental experiment for inspection of cooling pipes in operation by using ultrasonic technique. Fusion Eng Des 2006;81(8–14):1583–7.
[4] Romanoni M, Gonella S, Apetre N, Ruzzene M. Two-dimensional periodic actuators for frequency-based beam steering. Smart Mater Struct 2009;18 (12):125023-1–19.
[5] Vasile CF, Thompson RB. Excitation of horizontally polarized shear elastic waves by electromagnetic transducers with periodic permanent magnets. J Appl Phys 1979;50(4):2583–8.
[6] Ogilvy J. Ultrasonic beam profiles and beam propagation in an austenitic weld using a theoretical ray tracing model. Ultrasonics 1986;24(6):337–47.
[7] Ogilvy J. Computerized ultrasonic ray tracing in austenitic steel. NDT&E Int 1985;18(2):67–77.
[8] Pardee WJ, Thompson R. Half-space radiation by EMATs. J Nondestruct Eval 1980;1(3):157–81.
[9] Jian X, Dixon S, Edwards R, Morrison J. Coupling mechanism of an EMAT. Ultrasonics 2006;44:e653–6 Proceedings of Ultrasonics International (UI05) and World Congress on Ultrasonics (WCU).
[10] Hirao M, Ogi H. An SH-wave EMAT technique for gas pipeline inspection. NDT&E Int 1999;32(3):127–32.
[11] Mirkhani K, Chaggares C, Masterson C, Jastrzebski M, Dusatko T, Sinclair A, et al. Optimal design of EMAT transmitters. NDT&E Int 2004;37(3):181–93.
[12] Gao H, Lopez B. Development of single-channel and phased array electromagnetic acoustic transducers for austenitic weld testing. Mater Eval 2010;68:821–7.
[13] Wooh S-C, Shi Y. Optimum beam steering of linear phased arrays. Wave Motion 1999;29(3):245–65.
[14] Ramm OV, Smith S. Beam steering with linear arrays. IEEE Trans Biomed Eng 1983;BME-30:438–52.
[15] Hill S, Dixon S. Frequency dependent directivity of periodic permanent magnet electromagnetic acoustic transducers. NDT&E Int 2014;62:137–43.
[16] Somer J. Electronic sector scanning for ultrasonic diagnosis. Ultrasonics 1968;6 (3):153–9.
[17] Holmes C, Drinkwater B, Wilcox P. Post-processing of the full matrix of ultrasonic transmit-receive array data for non-destructive evaluation. NDT&E Int 2005;38:701–11.
[18] Cohen L. Time–frequency distributions—a review. Proc. IEEE 1989;77 (7):941–81.
[19] Jones D, Parks T. A resolution comparison of several time–frequency representations. IEEE Trans Signal Process 1992;40(2):413–20.
[20] Niethammer M, Jacobs LJ, Qu J, Jarzynski J. Time–frequency representations of Lamb waves. J Acoust Soc Am 2001;109(5):1841–7.
[21] Edwards RS, Dixon S, Jian X. Enhancement of the Rayleigh wave signal at surface defects. J Phys D: Appl Phys 2004;37(16):2291–7.
[22] Ogilvy J. Model for the ultrasonic inspection of rough defects. Ultrasonics 1989;27:69–79.
[23] Ogilvy J, Culverwell I. Elastic model for simulating ultrasonic inspection of smooth and rough defects. Ultrasonics 1991;29(6):490–6.
[24] Zhang J, Drinkwater B, Wilcox P. Effect of roughness on imaging and sizing rough crack-like defects using ultrasonic arrays. IEEE Trans Ultrason Ferroelectr Freq Control 2012;59(5):939–48.
[25] Daubechies I. The wavelet transform, time–frequency localization and signal analysis. IEEE Trans Inf Theory 1990;36(5):961–1005.